Journal of Solid State Chemistry 184 (2011) 1293–1303

Contents lists available at ScienceDirect

Journal of Solid State Chemistry

journal homepage: www.elsevier.com/locate/jssc

Phase stability and chemical composition dependence of the thermoelectric properties of the type-I clathrate $Ba_8Al_xSi_{46-x}$ ($8 \le x \le 15$)

Naohito Tsujii [a,b,*], John H. Roudebush [b], Alex Zevalkink [c], Catherine A. Cox-Uvarov [b], G. Jeffery Snyder [c], Susan M. Kauzlarich [b]

[a] National Institute for Materials Science, 1-2-1 Sengen, Tsukuba 305-0047, Japan
[b] Department of Chemistry, University of California, One Shields Avenue, Davis, CA 95616, USA
[c] Materials Science, California Institute of Technology, 1200 California Blvd, Pasadena, CA 91125, USA

ARTICLE INFO

Article history:
Received 11 November 2010
Received in revised form
10 March 2011
Accepted 20 March 2011
Available online 5 April 2011

Keywords:
Clathrate compounds
Phase relation
Thermoelectric property

ABSTRACT

Phase stability of the type-I clathrate compound $Ba_8Al_xSi_{46-x}$ and the thermoelectric property dependence on chemical composition are presented. Polycrystalline samples were prepared by argon arc melting and annealing. Results of powder X-ray diffraction and electron microprobe analysis show that the type-I structure is formed without framework deficiency for $8 \le x \le 15$. Lattice constant a increases linearly with the increase of x. Thermoelectric properties were measured for $x=12$, 14 and 15. The Seebeck coefficients are negative, with the absolute values increasing with x. The highest figure of merit $zT=0.24$ was observed for $x=15$ at $T=1000$ K, with carrier electron density $n=3\times10^{21}$ cm^{-3}. A theoretical calculation based on the single parabolic band model reveals the optimum carrier concentration to be $n\sim4\times10^{20}$ cm^{-3}, where $zT\sim0.7$ at $T=1000$ K is predicted.

1. Introduction

Inorganic clathrate structured compounds have been studied extensively as candidates for high temperature thermoelectric materials. One class of compounds with this structure type has frameworks built up by the electronegative main group elements, and electropositive ions that are within the cages of the framework. The framework is made through strong covalent bonds of the main group elements. The strong covalency indicates significant overlap of the *s–p* hybridized orbitals, which leads a high mobility of electrons or holes. In addition, the cages are large enough for cations to rattle or to occupy one of the disordered positions, thereby helping to reduce the thermal conductivity. Clathrate compounds are thus considered to be ideal materials for thermoelectric applications as the idea of 'electron–crystal, phonon–glass' can be realized [1].

The type-I clathrates with the formula of $A_8B^{13}_{16}B^{14}_{30}$, where A, B^{13}, and B^{14} are alkaline earth metals, 13, and 14 group metals, respectively, are particularly interesting. This class of compounds forms a cubic structure with the space group $Pm\text{-}3n$, shown in Fig. 1. There are three different crystallographic sites in the framework identified by their Wyckoff symmetry notation as 6*c*, 16*i*, and 24*k*. Each of the sites is tetrahedrally coordinated by other framework atoms. Assuming that two electrons are transferred from one alkaline earth metal to the framework sites, the compound should meet the Zintl condition; each of the framework sites has 4 valence electrons necessary to form the tetrahedral bonding coordination around the atom. As a result, they are expected to have an energy gap around the Fermi energy, thereby a large Seebeck effect is expected. Indeed, Nolas et al. [2] observed semiconducting behavior in $Sr_8Ga_{16}Ge_{30}$ with a relatively high electrical conductivity and a large Seebeck coefficient. Furthermore, they discovered a glass-like thermal conductivity [2,3]. This leads the compound to be a very promising thermoelectric material with a high thermoelectric figure of merit, zT, and inspiring further investigation into the thermoelectric properties of a number of inorganic clathrate compounds with the same structure [4].

Most investigated so far are Ge- or Sn-based type-I clathrate compounds. Electronic structure calculations suggested the band gap of 0.6–0.9 eV [5,6]. Most samples show a large negative Seebeck coefficient with metallic electrical resistivity, indicating a degenerate *n*-type semiconductor, and a very small thermal conductivity of the order of 1 Wm^{-1} K^{-1} is observed [7–11]. Chemical composition dependence of the thermoelectric properties suggested that the carrier concentration decreases systematically in $Ba_8Ga_xGe_{46-x}$, $Sr_8Ga_xGe_{46-x}$ and $Ba_8Al_xGe_{46-x}$ when x is increased toward the Zintl condition $x=16$, and the thermoelectric properties become improved accordingly [12–14]. Indeed, samples with optimized x show high zT close to 1 around 900 K [9–12,15–17]. Notably, high thermoelectric performance has also been observed for p-type crystals with $x>16$ [12,18,19]. Besides,

* Corresponding author at: National Institute for Materials Science, 1-2-1 Sengen, Tsukuba 305-0047, Japan.
E-mail address: tsujii.naohito@nims.go.jp (N. Tsujii).

0022-4596/$ - see front matter © 2011 Elsevier Inc. All rights reserved.
doi:10.1016/j.jssc.2011.03.038

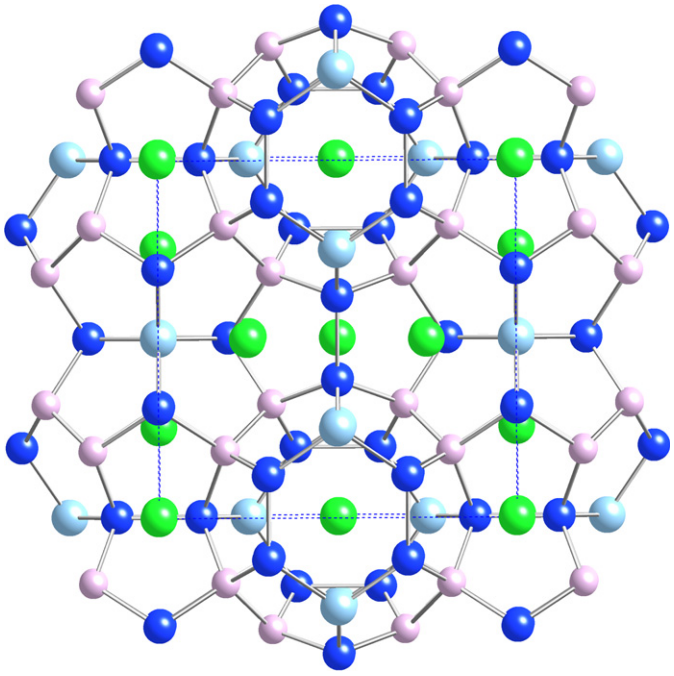

Fig. 1. Crystal structure of the type-I clathrate. The Ba sites are green. Si and Al atoms occupy 6*c*, 16*i*, and 24*k* sites. The 6*c* sites are light blue. The 16*i* sites are pink. The 24*k* sites are dark blue. (For interpretation of the references to color in this figure legend, the reader is referred to the web version of this article.)

an extremely low thermal conductivity was observed for β-$Ba_8Ga_{16}Sn_{30}$ [20].

In these clathrate compounds, deviation of the chemical composition from the Zintl condition easily occurs, which yields extra carriers and degrades the thermoelectric properties. Blake et al. [21] have demonstrated that direct bondings of the group-13 atoms are energetically unstable in these clathrates. Hence precise control of the stoichiometry becomes difficult with increasing the goup-13 element concentration toward the Zintl condition $x \sim 16$. Systematic studies of phase relation and careful chemical composition dependence of the properties are therefore quite important for the clathrate compounds.

This is especially true for the Si-based clathrate compounds. Although the literature reported the existence of four Si-based type-I clathrate compounds $A_8B^{13}_{16}Si_{30}$ with A=Sr, Ba and B^{13}=Al, Ga [22], only $Ba_8Ga_{16}Si_{30}$ has been well characterized and has been demonstrated to show a high thermoelectric performance [3,7,23,24]. For the other silicides, existence of the stoichiometric compound has not been verified. Trials to reproduce the $Sr_8Al_{16}Si_{30}$ phase were unsuccessful, resulting in the formation of $SrAl_2Si_2$ as the majority phase [25]. Thus the type-I Sr–Al–Si phase can be stabilized in a different stoichiometry [26]. Similarly, the $Sr_8Ga_xSi_{46-x}$ compounds were found to exist in the composition range of $11 \le x \le 14$ [27,28], and the Seebeck coefficients in these Sr–Ga–Si clathrates are low [29,30].

For the Ba–Al–Si ternary system, the phase relation against the chemical composition is still unclear. Mudryk et al. [31] studied the electrical resistivity and the Seebeck coefficient using polycrystalline samples with nominal compositions of $Ba_8Al_8Si_{36}$, $Ba_8Al_{12}Si_{33}$, and $Ba_8Al_{16}Si_{30}$. In this study, they adopted the chemical formula $Ba_8Al_xSi_{42-(3/4)x}\square_{4-(1/4)x}$, where $\square$ indicates a defect site in the framework. Although the defect composition was intended to meet the Zintl condition, these compounds showed metallic conductivity [31,32], and therefore may have had the vacancies filled, providing electrons in the conduction band [33]. Later, Al-flux technique resulted in large single crystalline samples of type-I Ba–Al–Si clathrate [34–38]. Chemical composition analysis for these crystals indicated the formula close to $Ba_8Al_{14}Si_{31}\square_1$, suggesting the existence of one defect site in the framework per unit cell [35]. Reported physical properties measurements for $Ba_8Al_{14}Si_{31}\square_1$ showed metallic conductivity, with a higher thermal conductivity and lower Seebeck coefficient than those of $Ba_8Ga_{16}Ge_{30}$. As a consequence, the figure of merit was $zT \sim 0.35$ at 1000 K.

Although these thermoelectric performance values of Ba–Al–Si clathrate compounds are lower than those observed for other clathrate compounds, there are significant advantage in the Ba–Al–Si compound from practical reasons. Aluminum and silicon are quite abundant; hence, much cheaper than Ga, In, Ge, or Sn. The melting point of the Ba–Al–Si system is reported to be around 1360 K [22,35,36], which is higher than that ($\sim$1230 K) for the Ba–Ga–Ge system [22]. The lighter weight of the former is also preferable for applications such as those in the transportation industry. It is important to elucidate how the thermoelectric performance in the Ba–Al–Si clathrate compounds can be improved. In the previous work on $Ba_8Al_{16}Si_{30}$ by Mudryk et al. [31,32], precise chemical composition analysis was not performed, thereby more systematic studies are needed for the Ba–Al–Si phase relation. Recent band structure calculation suggested that $Ba_8Al_{16}Si_{30}$ should be a narrow gap semiconductor [39], in contrast to the metallic conductivity experimentally observed. This discrepancy may be due to a deviation in the chemical composition from the ideal Zintl composition.

To clarify the phase stability of the type-I clathrate Ba–Al–Si phase, we began by synthesizing polycrystalline samples, and verifying structures and chemical compositions using X-ray diffraction and electron microprobe analysis. Here we adopted the formula $Ba_8Al_xSi_{46-x}$, aiming to obtain type-I Ba–Al–Si compounds free from the framework deficiency. The number of conduction electrons for $Ba_8Al_xSi_{46-x}$ should change systematically as a function of x, and the lattice contribution in the thermal conductivity is expected to be unchanged if framework or cation site deficiency is ruled out. This allows us to discuss the possibility of the existence of the stoichiometric phase of $Ba_8Al_{16}Si_{30}$ and to predict the thermoelectric properties when it is optimized.

2. Experimental section

2.1. Synthesis

Polycrystalline samples of $Ba_8Al_xSi_{46-x}$ were prepared by arc melting in argon from pure elements and subsequent annealing. Attempts were made to prepare samples with x=6, 8, 10, 12, 14, 15, and 16. Metals of Ba (99.9%, Johnson Matthey Co.), Al (99.999%, Furuchi Chem. Co., Japan), and Si (better than 99.9999%, Furuchi Chem. Co., Japan) were weighed. Since Ba is more volatile than the other two elements, an extra amount (up to 1.2%) of Ba was loaded. As will be described later, the chemical composition analysis revealed that samples have almost stoichiometric composition, i.e., Ba:(Al+Si)=8:46, indicating this addition of extra Ba worked as expected. Hence, we will hereafter use the notation $Ba_8Al_xSi_{46-x}$, neglecting the additional amount of Ba. Barium specimens were kept and weighed inside a dry box filled with N_2 with water vapor less than 1 ppm. The arc furnace chamber was evacuated to vacuum for more than 30 min and filled with pure argon (99.99%). This was repeated several times. Zirconium was melted in the arc chamber in advance to the reaction of the samples in order to absorb any oxygen. Then the elements of Ba, Al, and Si were melted on a water-cooled copper hearth. After melting the metals, the sample ingots were reversed and melted again to obtain good homogeneity. This process was

repeated four times. The decreased weight was less than 1% of the ideal mass.

As-cast samples thus prepared were placed in alumina crucibles, which were sealed under vacuum in quartz tubes. The tubes were then heated in an electric furnace at 1020–1270 K for several days, and removed from the furnace allowing them to cool rapidly to room temperature. These annealed samples were polished with sand papers to remove any oxidized surface.

Sintered samples were prepared for thermoelectric measurements. Polycrystalline samples with $x=12$, 14 and 15 were synthesized by argon arc melting and annealing similarly. The polycrystalline ingots were polished so that the oxidized surface was removed, and were put into a tungsten-carbide lined methacrylate ball mill vial under N_2 atmosphere. The ingots were crushed into powder by ball milling for 10 min. Coarse grains inside the powder were removed by sieves. The fine powders thus obtained were put into a high density graphite die with the diameter of 12.0 mm. These procedures were performed in a dry box. Then the carbon dies were pressed up to 44.2 MPa and heated under vacuum by means of spark plasma sintering method at 1070 K for 5 min. Densities of the pellets were measured by the Archimedes principle and found to be 91–96% of the theoretical values.

2.2. Powder X-ray diffraction

Both the as-cast and the annealed samples were measured by powder X-ray diffraction (XRD). A Bruker diffractometer operating at 40 kV and 40 mA with Cu $K\alpha$ radiation (1.54056 Å) was employed with a rotating sample holder to reduce the orientation effect. XRD patterns were analyzed by means of the Rietveld method to obtain lattice constants of the phase using RIETAN-FP program [40,41].

2.3. Microprobe analysis

Electron microprobe analysis was performed to verify the chemical composition of the samples. Annealed samples were polished to a mirror-like finish. The samples were then placed in a Cameca SX-100 electron microprobe. Net elemental intensities for Al and Si were determined with respect to pure Al and Si, while that for Ba was measured by a single-crystal of $Ba_{19.94}Al_{72.02}Si_{8.04}$ [36]. The microprobe was operated with an accelerating voltage of 20 keV and the electron current of 10 nA. The sum of the determined values of weight % for each element was $100\pm0.5\%$, indicating that the calibration is reasonable. Chemical composition was investigated for four different points on each phase of the samples, and the results were consistent with each other.

2.4. Differential scanning calorimetry (DSC) measurement

A Netzsch Thermal Analysis STA 409 was used to measure the thermal properties of $Ba_8Al_xSi_{46-x}$ $x=12$, 14, and 15 samples after SPS pressing. A small piece of the SPS pellet (~30 mg) was placed in an alumina crucible with cover. Prior to sample measurement, the crucible was used to establish a baseline reading for the temperature regime. The instrument chamber was evacuated and purged with Ar multiple times before each measurement. Samples were heated under flowing argon from room temperature to 1473 K at 10 K/min and data collection was 4 pts/K.

2.5. Thermoelectric properties measurements

The spark plasma sintered (SPS) pellets with diameter of 12 mm and thickness of 1 mm were used for the measurements. Thermoelectric properties were measured under dynamic vacuum. The Seebeck coefficient (α) was measured by the differential light-pipe method using W/Nb thermocouples. The electrical resistivity (ρ) was measured using the van der Pauw technique with a current of 100 mA. The Hall coefficient (R_H) was measured with a magnetic field of 2 T. The carrier concentration (n) was estimated under the assumptions of single carrier type and a scattering factor of 1.0 by $n=1/R_He$, where e is the electron charge. The Hall mobility (μ) was calculated from the Hall coefficient and the resistivity with $\mu=R_H/\rho$. The thermal diffusivity D_T was measured using a laser-flash method. The thermal conductivity κ was calculated using $\kappa=D_TC_pd$, where d is the geometrical density of the sample and C_p the heat capacity. We employed the Dulong–Petit approximation for C_p.

3. Results and discussion

3.1. Phase relation of $Ba_8Al_xSi_{46-x}$ with the type-I structure

Fig. 2 shows the powder X-ray diffraction (XRD) patterns of the as-cast samples of $Ba_8Al_xSi_{46-x}$ with $x=6$, 8, 10, 12, 14, and 16.

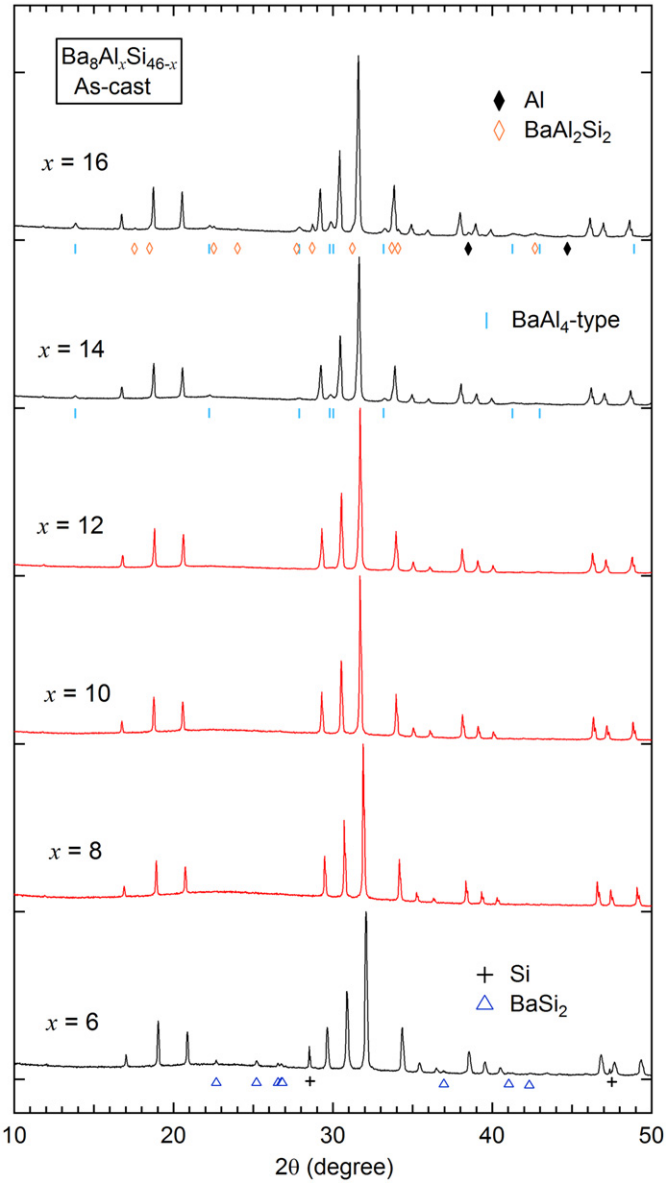

Fig. 2. Powder X-ray diffraction patterns of as-cast samples of $Ba_8Al_xSi_{46-x}$.

For $x=8$–12, the XRD patterns are well explained by a type-I clathrate phase. As-cast samples are direct products out of the liquid phase, thereby the single phased XRD pattern indicates that the type-I $Ba_8Al_xSi_{46-x}$ phase melts congruently for $x=8$–12. For $x=6$, the XRD pattern was indexed mainly by type-I phase with minor peaks. These peaks were consistent with Si and orthorhombic $BaSi_2$ with the space group *Pnma*. For $x=14$, the XRD patterns showed type-I clathrate phase as the main phase, but with some minor peaks as well. Those peaks were indexed to be due to $BaAl_4$-type structure, space group *I*4/*mmm*, as shown in the Fig. 2. For $x=16$ as-cast sample, diffraction peaks from minor phases are further enhanced. In Fig. S1 in Supplementary Information, we show the result of Rietveld fitting for XRD pattern of the $x=16$ as-cast sample. The XRD pattern is explained by the type-I clathrate phase (*Pm*-3*n*) with lattice constant $a=10.5900(2)$ Å, and by $BaAl_4$-type phase, $BaAl_2Si_2$, and Al. The peak positions of these minor phases are also indicated in Fig. 2 by markers. $BaAl_2Si_2$ is reported to crystallize in three types of space groups, *Cmcm* and *Pnma* at ambient pressure, and *I*4/*mmm* under high pressure [42,43]. Calculated powder XRD patterns for $BaAl_2Si_2$ with the space group *Cmcm* and *Pnma* are quite similar, and the peak intensity of the minority phase in Fig. 2 is not sufficient to distinguish which type of $BaAl_2Si_2$ is formed in our samples. We then adopted *Pnma* for the space group of the $BaAl_2Si_2$ as the minority phase.

The existence of multiple phases for the nominal composition of $x=16$ indicates that the sample with this chemical composition melts incongruently, as previously pointed by Mudryk et al. [31]. For that case, annealing is needed for homogenization. In Fig. 3, the powder XRD patterns for the annealed $Ba_8Al_xSi_{46-x}$ are shown. A very broad scattering is seen around $2\theta=15$–25°, which is due to the glass sample holder. Again the patterns for $x=8$, 10, and 12 agreed with the type-I structure, and we omit the patterns for $x=10$ and 12 in Fig. 3. Instead, we show the XRD patterns of the annealed samples in Fig. S2 in Supplementary Information with the Rietveld fitting results. For $x=6$, the powder XRD pattern consists of three phases, the type-I clathrate as the main phase, and minor phases of Si and $BaSi_2$. This was qualitatively similar to that of the as-cast sample. In addition, the lattice parameter of the type-I phase in the $x=6$ annealed sample, $a=10.4912$ Å is very close to $a=10.4868$ Å for $x=8$ annealed sample. This suggests that $x=8$ is the lower composition limit for Al in the type-I structure.

For $x=14$, samples were annealed at 870, 1020, or 1070 K for 5 days, each of which showed the existence of $BaAl_2Si_2$ as a minority phase. Then we annealed the sample at 1170 K for 3 days. As is shown in Fig. 3, annealing at 1170 K yielded a pure XRD pattern of the type-I phase with negligible $BaAl_2Si_2$. For $x=15$ and 16, annealing at 870, 1020, 1070, or 1170 K did not eliminate the minor phases, and XRD patterns still showed the existence of $BaAl_2Si_2$. Then the samples were further annealed at 1270 K, which is close to the melting point of $BaAl_2Si_2$ [42]. The XRD pattern of the sample annealed at 1270 K appears much improved, with only a trace amount of $BaAl_2Si_2$ peaks. Although the XRD pattern for the annealed $x=16$ sample in Fig. 3 appears to be pure, the lattice parameter $a=10.63190(7)$ Å is almost the same as that for $x=15$ annealed sample, $a=10.63220(9)$ Å. The lattice constant a is found to increase from 10.4868 to 10.6322 Å when Al concentration is increased from $x=8$ to 15. Thus the actual chemical composition of $x=16$ annealed sample is likely to be deviated from the nominal composition. Indeed, the microprobe analysis revealed the sample still contains $BaAl_2Si_2$ and Al, and the stoichiometry of the type-I phase is close to $x=15$.

In Fig. 4, the backscattering electron images (BEI) obtained by the electron microprobe study are shown. The chemical composition determined from this study is listed in Table 1. For $x=6$, small crystals with typical size of about 10 μm can be seen distributed

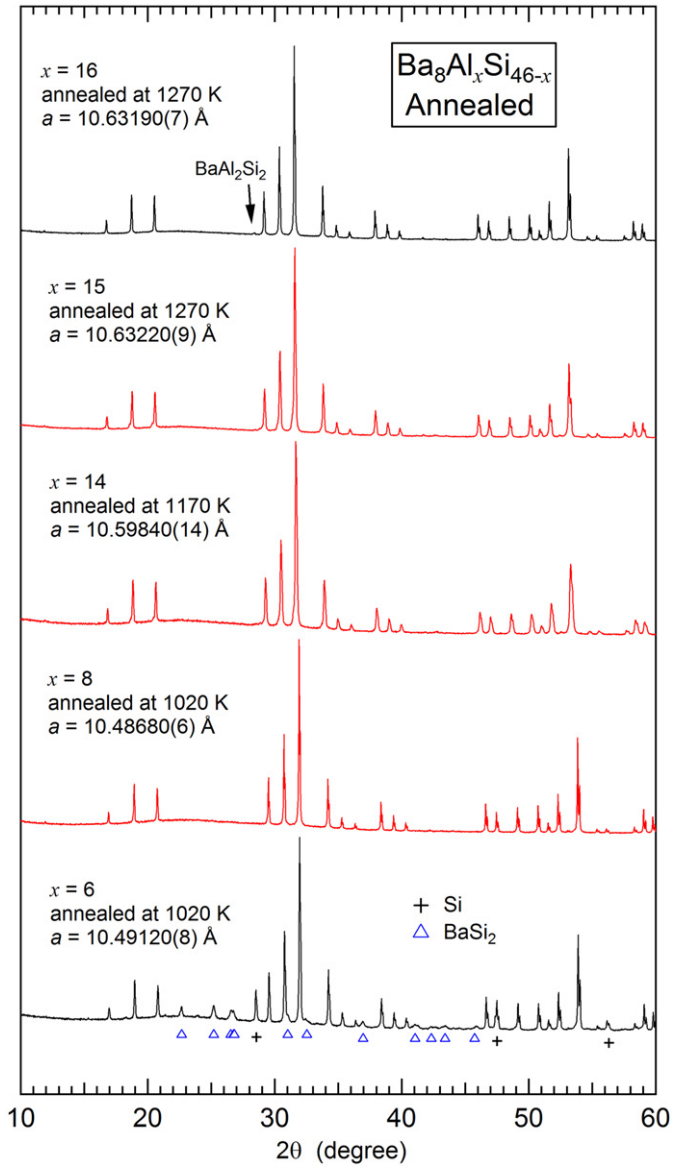

Fig. 3. Powder X-ray diffraction patterns of annealed samples of $Ba_8Al_xSi_{46-x}$.

over the surface. Chemical composition analysis for three crystals indicated that these are Si with purity higher than 99.5%. The microprobe analysis did not find $BaSi_2$ phase in the $x=6$ sample, though the powder XRD pattern in Fig. 3 revealed its existence. We speculate that the $BaSi_2$ phase decomposed into $Ba(OH)_2$ and Si with water during the surface polishing, which increased the amount of Si around the surface. The chemical composition of the majority phase was Ba:Al:Si=14.66(6):14.94(6):70.40(6) at %, which is expressed as $Ba_{7.90(4)}Al_{8.06(3)}Si_{37.94(3)}$. Here we employed the chemical formula $Ba_zAl_xSi_{46-x}$, assuming there are no defects in the framework site. If the value of z is larger than 8, it means the existence of framework deficiency, as the type-I structure contains only 8 cavities per formula unit where the cation can be inserted. Now the value of z is very close to, and even smaller than 8. Thus we can conclude that the framework deficiency is absent in this phase, and the barium site is almost fully (~98.7%) occupied. On the other hand, the Al concentration, $x=8.06$, determined by the microprobe analysis is significantly larger than the nominal value of $x=6$. Since the XRD pattern of this annealed sample showed the coexistence of Si and $BaSi_2$, the deviation of the chemical composition from the nominal value is reasonable. Moreover, this indicates that the

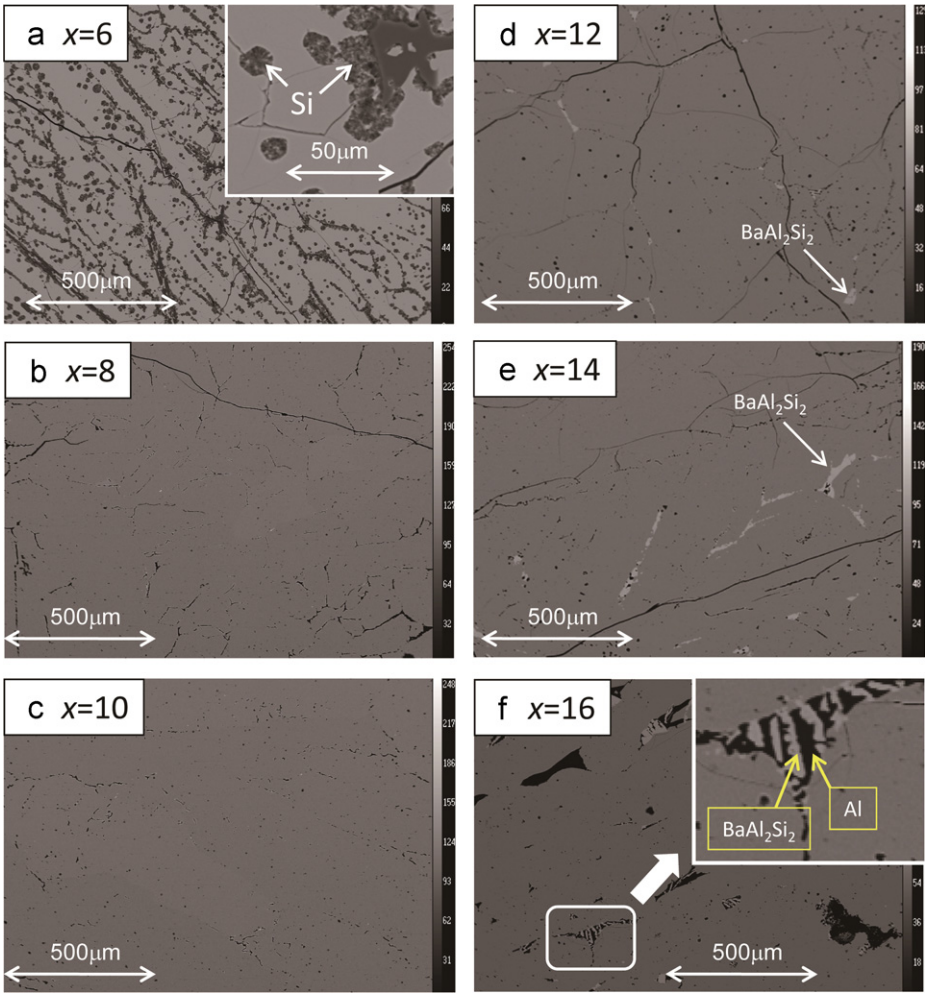

Fig. 4. Backscattering electron image (BEI) from the electron microprobe analysis for annealed samples of $Ba_8Al_xSi_{46-x}$. (a) $x=6$ annealed at 1020 K, (b) $x=8$ annealed at 1020 K, (c) $x=10$ annealed at 1020 K, (d) $x=12$ annealed at 1020 K, (e) $x=14$ annealed at 1170 K, (f) $x=16$ annealed at 1270 K. Inset in (a) shows an enlarged image, where small crystals are assigned to be Si. Inset in (f) shows an enlarged image of an eutectic region, where black (mainly composed of Al) and white (almost $BaAl_2Si_2$) regions coexist.

Table 1
Chemical composition of the main phase of the annealed $Ba_8Al_xSi^{46-x}$ samples determined from electron probe microanalysis (EPMA). Standard deviations are indicated as numbers inside parentheses. The chemical formula is expressed in $Ba_zAl_xSi_{46-x}$.

	Atomic percent composition				Chemical formula
	Ba	Al	Si	Sum	
$x=6$	14.66(6)	14.94(6)	70.40(6)	100.00	$Ba_{7.90(4)}Al_{8.06(3)}Si_{37.94(3)}$
$x=8$	14.68(6)	14.92(9)	70.40(10)	100.00	$Ba_{7.92(4)}Al_{8.04(5)}Si_{37.96(5)}$
$x=10$	14.69(5)	18.66(9)	66.66(9)	100.01	$Ba_{7.92(3)}Al_{10.06(5)}Si_{35.94(5)}$
$x=12$	14.71(5)	21.60(57)	63.70(58)	100.01	$Ba_{7.93(3)}Al_{11.65(31)}Si_{34.35(31)}$
$x=14$	14.72(4)	26.41(38)	58.87(38)	100.00	$Ba_{7.94(3)}Al_{14.25(21)}Si_{31.75(21)}$
$x=16$ #1	14.74(5)	27.41(8)	57.84(9)	99.99	$Ba_{7.96(3)}Al_{14.79(4)}Si_{31.21(4)}$
$x=16$ #2	14.72(4)	27.69(10)	57.60(11)	100.01	$Ba_{7.94(3)}Al_{14.93(6)}Si_{31.07(6)}$

value of $x \cong 8$ is the lower limit of homogeneity range in which type-I $Ba_8Al_xSi_{46-x}$ can exist. This conclusion is consistent with the similar lattice constants of $x=6$ and 8 annealed samples, as discussed above.

Fig. 4(b)–(e) shows the backscattered electron image (BEI) of annealed $Ba_8Al_xSi_{46-x}$ with nominal $x=8$, 10, 12 and 14. They appear to be almost in a single phase as expected from the pure XRD patterns, though a tiny amount of minor phase is also seen. The chemical composition of the second phase was found to be $BaAl_2Si_2$, consistent with the XRD pattern. For the main part of these samples, their chemical compositions were expressed by using the notation $Ba_zAl_xSi_{46-x}$ to be $Ba_{7.92(4)}Al_{8.04(5)}Si_{37.96(5)}$, $Ba_{7.92(3)}Al_{10.06(5)}Si_{35.94(5)}$, $Ba_{7.93(3)}Al_{11.65(31)}Si_{34.35(31)}$, and $Ba_{7.94(3)}Al_{14.25(21)}Si_{31.75(21)}$, respectively. The values of z are again very close to and only slightly smaller than 8.0 when the number of the framework sites is fixed to 46, supporting that the framework deficiency is absent and the barium sites are almost fully (98.7%–99.5%) occupied. The values of $x=8.04$, 10.06, 11.65, and 14.25 are close to the nominal values.

In Fig. 4(f) is the BEI of #2 sample for the nominal composition of $Ba_8Al_{16}Si_{30}$. A stripe shaped structure is observed, which is

enlarged in the inset of Fig. 4(f). The chemical composition analysis showed the black and the white regions are Al with the purity of 98–99% and $BaAl_2Si_2$, respectively. The stripe structure suggests this region is formed from an eutectic melt of Al and $BaAl_2Si_2$. For the majority phase, the composition analysis is expressed by using the formula $Ba_zAl_xSi_{46-x}$ to be $Ba_{7.96(3)}Al_{14.79(4)}Si_{31.21(4)}$ for #1 sample, and $Ba_{7.94(3)}Al_{14.93(6)}Si_{31.07(6)}$ for #2 sample, both of which were annealed at 1270 K for 7 days. Thus the type-I phase formed has the chemical composition $x \leq 15$ even though larger amount of Al was loaded. The existence of Al/$BaAl_2Si_2$ eutectic region inside the sample implies that this is the maximum value of the Al concentration in the type-I $Ba_8Al_xSi_{46-x}$ clathrate. This is consistent with the lattice parameter for $x=15$ and 16 annealed samples, both of which have similar values of $a \sim 10.632$ Å as shown in Fig. 3. Thus our study indicates that the type-I $Ba_8Al_xSi_{46-x}$ phase without framework deficiency exists in the chemical composition range of $8 \leq x \leq 15$. It should be mentioned that the homogeneity range of $Ba_8Ga_xGe_{46-x}$ was reported to be $12 \leq x \leq 17$ [12], but later studies have shown that the composition range without framework vacancy can be much narrower [13,33]. More precise crystallographic investigations are needed to confirm the absence of framework deficiency in the present compounds.

In Fig. 5, the lattice constant a of the type-I $Ba_8Al_xSi_{46-x}$ is plotted as a function of x, where actual values of x are determined from the electron microprobe analysis. The values of a were obtained by Rietveld fittings of the annealed sample data shown in Fig. S2 in Supplementary Information. A linear relation of a and x is clearly seen. This in turn suggests that the lattice constant is a measure of the chemical composition as far as the deficiency in the framework and/or in the Ba site can be ruled out. Fitting the data resulted in a linear relation: $a=10.316(12)+0.0208(10)x$. Using this relation the hypothetical lattice parameter for the Zintl phase compound $Ba_8Al_{16}Si_{30}$ is expected to be $a=10.649$ Å. In contrast, none of the reports of the lattice constant for the type-I Ba–Al–Si phase meet this value. The value $a=10.6285(1)$ Å by Mudryk et al. [31] corresponds to $x=15.02$, very close to the one we obtained in the attempt to synthesize $x=16$. The first report for this compound by Eisenmann et al. [22] gave $a=10.6068(30)$ Å, which corresponds to a smaller value $x=13.98$. The lattice constant $a=10.6373$ Å was reported by Condron et al. [34] for $Ba_{7.5}Al_{13}Si_{29.2}$, which gives $x=15.45$. This value is too large and is understood to be due to the framework deficiency, since the above chemical composition is expressed as $Ba_8Al_{13.9}Si_{31.1}\square_1$ [35]. We therefore suggest that the low thermoelectric performances so far reported for $Ba_8Al_{16}Si_{30}$ are attributed to the deviation of the chemical composition from the ideal stoichiometry.

In Section 3.2 we will show the variation of thermoelectric properties of $Ba_8Al_xSi_{46-x}$ when x is varied from 12 to 15. The samples used for the thermoelectric measurements were pellets made by SPS from powder specimens of $Ba_8Al_xSi_{46-x}$ with nominal $x=12$, 14, and 15. The electron microprobe analysis for the SPS pellets yielded the chemical composition $Ba_{7.98(2)}Al_{11.97(10)}Si_{34.03(10)}$, $Ba_{7.92(11)}Al_{13.74(37)}Si_{32.26(37)}$, and $Ba_{8.02(4)}Al_{14.74(14)}Si_{31.26(14)}$, respectively. The Al contents were almost consistent with the nominal ones, thereby we refer to these SPS samples as $x=12$, 14 and 15. Although the $x=15$ SPS sample shows a Ba occupation number 8.02 slightly higher than 8, this deviation is within the error. Even if the Ba content 8.02 is normalized to be 8.0, the number of the framework sites is 45.9, very close to 46, therefore we do not take this possible framework deficiency into consideration. The lattice constants of these three samples are also plotted in Fig. 5, and are consistent with the linear relation between a and x. Powder XRD patterns of the SPS samples are shown in Fig. S3 in Supplementary Information. They are consistent with the type-I structure, with a small amount (up to 2%) of $BaAl_2O_4$ impurity phase and trace amount of Si. Peaks of $BaAl_2Si_2$ were not observed in the XRD patterns for the SPS samples, though $BaAl_2Si_2$ impurity is found in the annealed sample as shown in Fig. 4. $BaAl_2Si_2$ may be more easily oxidized during the SPS process than the clathrate compound. The effect of $BaAl_2O_4$ to thermoelectric power is considered to be of minor importance, since it is an electrical insulator. On the other hand, it can make the samples both electrically and thermally less conductive. However, we do not consider the effect because the volume fraction to the sample is small (~2%).

Fig. 6 shows DSC plots from 1100 to 1475 K for the $x=12$, 14, and 15 SPS samples. The endotherm peaks appear at 1422.1, 1408.2 and 1405.7 K while the exotherm peaks appear at 1383.0, 1359.6 and 1374.0 K for $x=12$, 14, and 15, respectively. The temperature dependence of the endotherms (melting) follow the expected trend based on x; the melting temperature decreases with the increase of Al content. On the other hand, the exotherm

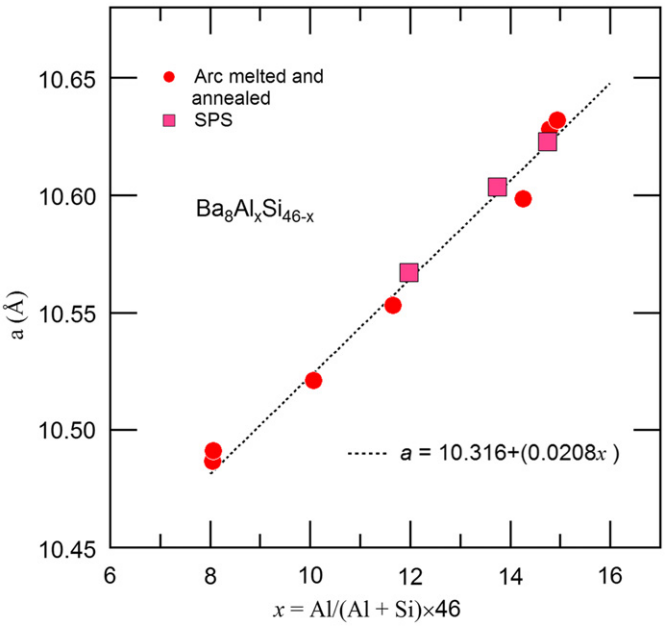

Fig. 5. Lattice constant a of annealed samples of $Ba_8Al_xSi_{46-x}$ as a function of x. The value of x was determined by the EPMA. The dotted line indicates the result of a linear fitting, which yields $a=10.316(12)+0.0208(10)x$.

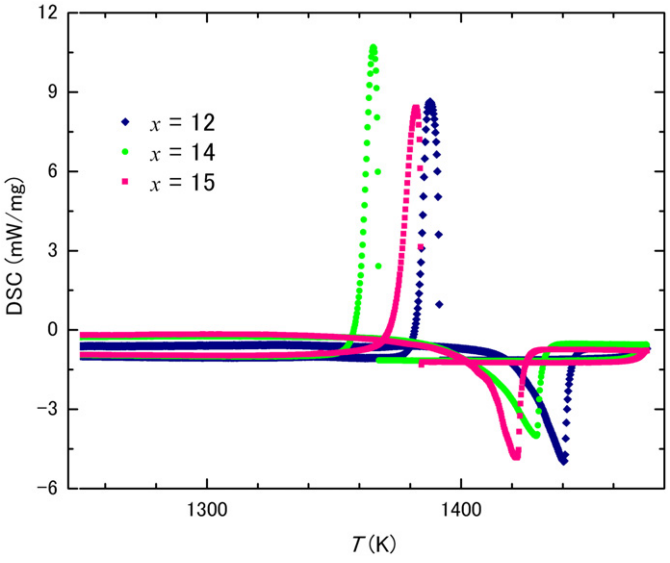

Fig. 6. DSC traces as a function of temperature for $Ba_8Al_xSi_{46-x}$.

(crystallization) temperature for $x=15$ is higher than that of $x=14$, and is close to the exotherm temperature for $x=12$. One possible explanation would be based on the fact that the sample with x close to 16 melts incongruently, and recrystallizes with minor phases such as $BaAl_4$, as suggested from the XRD pattern of the as-cast samples (Fig. 2 and Fig. S1). The melting temperature of $BaAl_4$ is reported to be $\sim$1370 K [44,45], in good agreement with the exotherm temperature 1374 K for $x=15$. Therefore at the exotherm of $x=15$, the crystallization of the $BaAl_4$ phase can start to occur. In that case, the Al concentration of the liquid phase is lowered than the nominal value, resulting in the formation of Si-rich clathrate phase. From the XRD pattern of the $x=16$ as-cast sample, lattice constant $a=10.5900(2)$ Å has been obtained, as is shown in Fig. S1 in Supplementary Information. This corresponds to the Al concentration $x\sim13.2$ for the clathrate phase. Therefore the exotherm temperature of $x=15$ sample can be attributed to the formation of $BaAl_4$ phase around 1370 K, followed by the recrystallization of clathrate phase with Al composition $x\sim13$, of which melting temperature is expected to be in-between those of $x=12$ and 14. The DSC data shown in Fig. 6 is consistent with this explanation.

3.2. Thermoelectric properties of $Ba_8Al_xSi_{46-x}$

Using the Zintl–Klemm charge-counting formalism, $Ba_8Al_{16}Si_{30}$ is expected to be a charge-balanced semiconductor. This is confirmed in first-principle calculations performed by Nenghabi and Myles [39] which predict a band gap with the Fermi level at the top the valence band. One would therefore expect $Ba_8Al_{16}Si_{30}$ to exhibit non-degenerate semiconducting behavior, with a large Seebeck coefficient (α), and a resistivity (ρ) decreasing with temperature due to intrinsic carrier activation. The samples presented here ($Ba_8Al_xSi_{46-x}$) have a maximum aluminum content $x=15$, which, assuming each missing Al atom contributes one free electron, corresponds to a predicted carrier concentration of 9×10^{20} cm^{-3}. Thus, one would expect the samples in this study ($x=12$, 14, and 15) to be n-type and to behave as highly degenerate semiconductors.

Indeed, high temperature electronic transport measurements of $Ba_8Al_xSi_{46-x}$ ($x=12$, 14, and 15) reveal negative Seebeck coefficients $\alpha(T)$ (shown in Fig. 7(a)), with magnitudes increasing linearly with temperature, indicative of degenerate semiconductor behavior. The magnitudes of $\alpha(T)$ increase with x, consistent with the decrease in carrier concentration expected as the composition of $Ba_8Al_xSi_{46-x}$ approaches toward the Zintl condition ($x=16$). The resistivity $\rho(T)$ of $Ba_8Al_xSi_{46-x}$ decreases as x decreases (Fig. 7(b)), which is also rationalized by the increase in carrier electrons associated with non-stoichiometry. For $x=12$–15, the temperature dependence of the resistivity is consistent with that expected for a degenerate semiconductor; increasing with temperature, presumably due to acoustic phonon scattering. The $x=15$ sample shows an anomaly in ρ(T) curve around 1000 K. Similarly, the $\alpha(T)$ show slight irreversible behavior around 1000 K. The origin of the anomalous behavior is unclear, though part of them may be due to the melting of tiny amount of aluminum at 930 K.

These chemical composition dependence of $\alpha(T)$ and $\rho(T)$ are similar to those observed in $Ba_8Ga_xGe_{46-x}$ [12,13,16,17], $Sr_8Ga_xGe_{46-x}$ [46] and $Ba_8Al_xGe_{46-x}$ [14], which show a negative $\alpha(T)$ and a metallic $\rho(T)$, with absolute values becoming prominent when x is increased toward 16. Some samples of $Ba_8Ga_xGe_{46-x}$ and $Sr_8Ga_xGe_{46-x}$ show a minimum in $\alpha(T)$ and a maximum in $\rho(T)$ at high temperature, with these extremum temperatures T_m decreasing when the carrier concentration becomes small [12,17,46]. This behavior is explained by a crossover to an intrinsic semiconductor at elevated temperatures, and is roughly characterized by the relation $E_g\sim2e\alpha(T_m)T_m$, where E_g and e are the energy gap and the electron charge, respectively [47]. We measured $\alpha(T)$ and $\rho(T)$

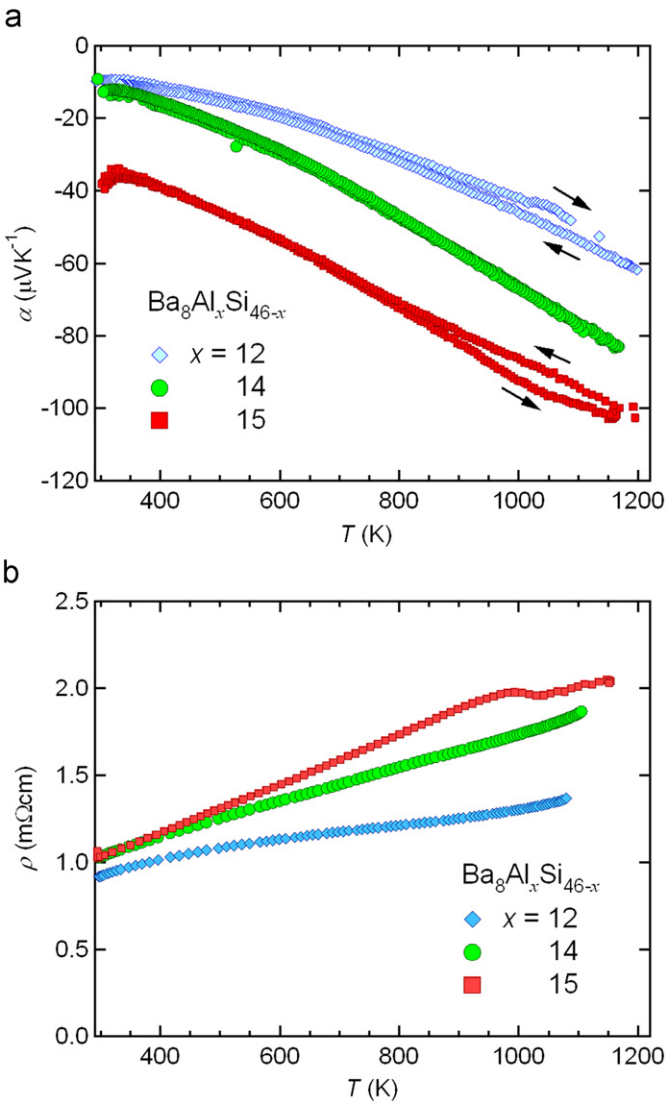

Fig. 7. Temperature dependence of the Seebeck coefficient α (a) and of the electrical resistivity ρ (b) of $Ba_8Al_xSi_{46-x}$.

for $x=15$ up to 1200 K, and such extrema are not observed yet. The values $\alpha\sim100$ μV/K at $T=1200$ K gives $2e\alpha(T)T=0.24$ eV. This value is smaller than $E_g\sim0.37$ eV, calculated by the local density approximation (LDA) for $Ba_8Al_{16}Si_{30}$ [39], consistent with the absence of extrema in our data. Nenghabi and Myles [39] pointed that the LDA calculations usually underestimate the band gaps, thereby actual energy gap of $Ba_8Al_xSi_{46-x}$ can be much larger. Thus it is expected that the absolute values of $\alpha(T)$ and $\rho(T)$ for the present samples of $Ba_8Al_xSi_{46-x}$ increase constantly up to its melting temperature, $\sim$1350 K.

Hall measurements of the $x=15$ sample reveal an n-type carrier concentration of $n=3\times10^{21}$ cm^{-3}, which remains constant with temperature. The result of the Hall measurement is shown as Fig. S5 in the Supplementary Information. The carrier concentration of the previously studied compound, $Ba_8Al_{14}Si_{31}\square_1$, is comparable to that of the $x=15$ sample, despite the disparity in stoichiometry [36]. A room temperature mobility of $\mu=1.5$ cm^2/Vs for the $x=15$ sample is calculated from the measured resistivity and carrier concentration ($\rho=1/ne\mu$). The mobility is expressed as $\mu=e\tau/m^*$, where τ and m^* are the carrier relaxation time and the electron effective mass, respectively. As is shown later, the effective mass for $x=15$ SPS sample is estimated to be $2.7m_e$, with m_e the electron mass. Now employing $\tau=10^{-14}$ s as a typical value [5], we obtain

μ=6.4 cm^2/Vs. Our result (1.5 cm^2/Vs) is smaller than this estimation, and partly it can be attributed to scattering at the grain boundary, especially the $BaAl_2O_4$ impurities. To estimate the carrier concentrations for the samples with x=12 and 14, we assume that the electron mobility remains fixed with respect to x, which is generally a reasonable assumption at high carrier concentrations. Using a mobility of 1.5 cm^2/Vs for the x=14 and x=12 sample yields estimated carrier concentrations of 4.0×10^{21} cm^{-3} and 4.6×10^{21} cm^{-3}, respectively.

The temperature dependence of the thermal conductivity (κ_{total}) is shown in Fig. 8(a). We employed the Dulong–Petit approximation for C_p to derive κ from the measured thermal diffusion. Utilizing this approximation is only verified for temperatures well above the Debye temperature θ_D. Now θ_D of $Ba_8Al_xSi_{46-x}$ is estimated to be about 450 K [4]. Thus the Dulong–Petit approximation would be valid to discuss the thermal properties at high temperature near 1000 K. However, it is to be noted that the approximation can underestimate C_p by 10–20%, which can yield overestimates in zT to the same extent [10,48]. Moreover, thermoelectric properties measurements at high temperature can generally contain uncertainty of 5–20% in each measurement, i.e., Seebeck coefficient, electrical resistivity, thermal diffusion, and temperature dependent sample density [11]. All these uncertainty can add up to a possible error in zT by about 50% [49].

κ_{total} is found to decrease with the increase of x across the measured temperature range. Since the total thermal conductivity includes both electron-mediated thermal conductivity, κ_e, and the lattice contribution, κ_l, the decrease of κ_{total} can mainly be attributed to the decrease of κ_e as the chemical composition is varied from x=12 to 15. Consistent with the lower resistivity found in the previous study of $Ba_8Al_{14}Si_{31}\square_1$, the total thermal conductivity of the x=15 sample in this study is smaller than that of $Ba_8Al_{14}Si_{31}$ (κ_{total}=2.4 W/Km at 400 K and 3 W/Km at 1200 K) [36]. Fig. 8(b) shows the temperature dependence of κ_e, determined using the Wiedemann–Franz relation, $\kappa_e=LT/\rho$. Here, we use temperature dependent Lorenz numbers (L) calculated using the equation,

$$L=\frac{k_B^2}{e^2}\frac{3F_0(\eta)F_2(\eta)-2F_1(\eta)^2}{F_0(\eta)^2}, \quad (1)$$

which employs a single parabolic band model. Here, η is the reduced chemical potential. $F_j(\eta)$ is the Fermi integral given as:

$$F_j(\eta)=\int_0^\infty \frac{\xi^j d\xi}{1+\exp[\xi-\eta]}. \quad (2)$$

η is determined by the experimental Seebeck coefficient of each sample at various temperatures, according to the following equation,

$$\alpha=\frac{k_B}{e}\left(\frac{(2+\lambda)F_{1+\lambda}(\eta)}{(1+\lambda)F_\lambda(\eta)}-\eta\right). \quad (3)$$

In both Eqs. (1) and (3), acoustic phonon scattering is taken as the dominant scattering mechanism (λ=0), which is reasonable at high temperatures [17].

The resulting temperature-dependent Lorenz numbers are plotted in the inset of Fig. 8(b). They vary from 2.4×10^{-8} WΩK^{-2} at room temperature to 1.9×10^{-8} WΩK^{-2} at 1100 K. This is in contrast to $L=2.44\times10^{-8}$ WΩK^{-2}, which is the value expected for free electrons and generally assumed for degenerate semiconductors as well. Our calculation for L is in good agreement with that previously obtained for $Ba_8Ga_{16}Ge_{30}$ [17]. The assumption of λ=0 would be valid for many clathrate compounds when high temperature properties are concerned. Thus using the free electron value $L=2.44\times10^{-8}$ WΩK^{-2} may have given overestimated κ_e in many cases, thereby underestimated κ_l, as was pointed in Ref. [17]. Although this does not affect the zT derived from the experimental data, it modifies expected zT value at optimized carrier concentration.

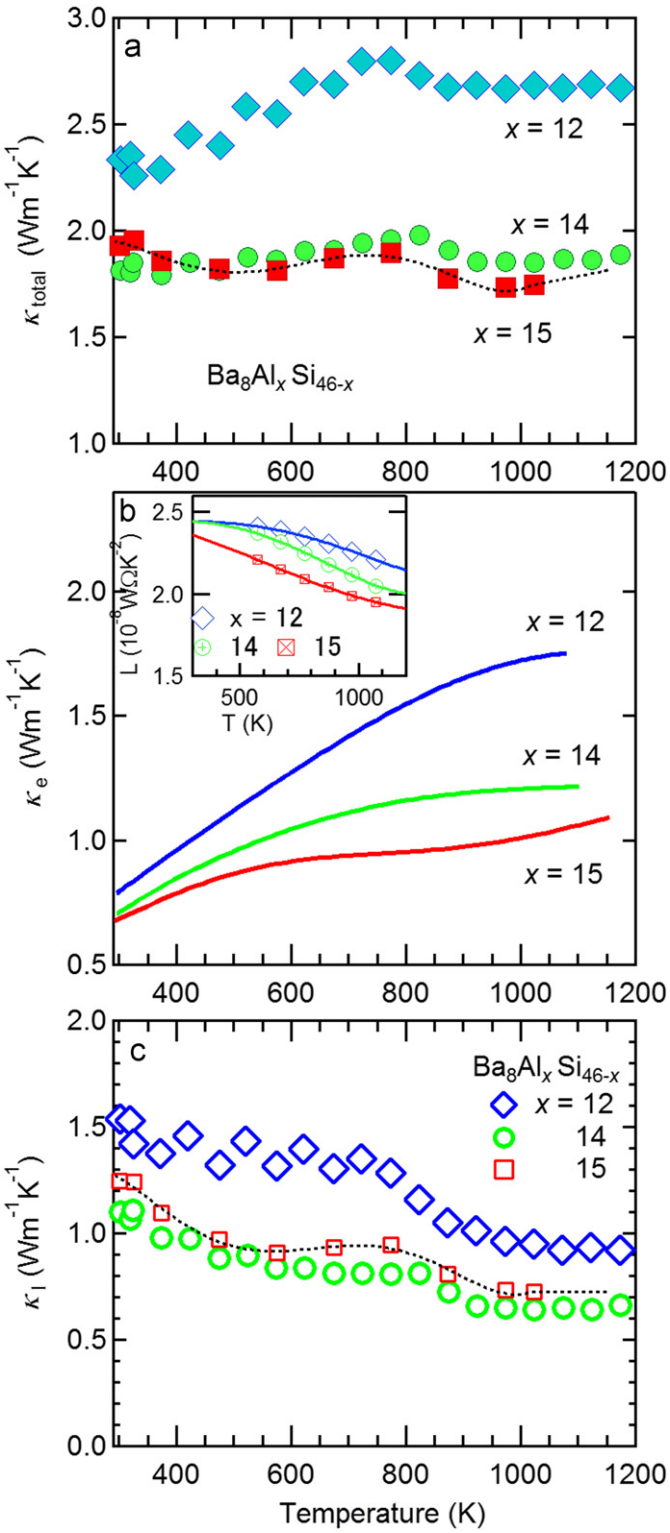

Fig. 8. (a) Temperature dependence of the thermal conductivity of $Ba_8Al_xSi_{46-x}$ (b) Temperature dependence of the electron contribution to thermal conductivity, κ_e calculated by the Wiedemann–Franz relation $\kappa_e=LT/\rho$, where L is a Lorenz number. (c) Temperature dependence of the lattice thermal conductivity κ_l, obtained from $\kappa_l=\kappa_{total}-\kappa_e$. The dashed line in (c) is the extrapolation of the lattice thermal conductivity for x=15, κ_L^{ex}, where κ_L above 1000 K is assumed to be a constant. The dashed line in (a) is the extrapolated thermal conductivity κ^{ex} for x=15 calculated by $\kappa_{total}^{ex}=\kappa_l^{ex}+\kappa_e$.

The lattice thermal conductivity is then obtained from $\kappa_l=\kappa_{total}-\kappa_e$, and is plotted in Fig. 8(c). Across all temperatures, the lattice thermal conductivity of these clathrates is exceptionally

low, comparable to that of $Ba_8Ga_{16}Ge_{30}$ calculated using similar methods [17] or to those in a number of Zintl compounds [33]. It is also possible that slight amount of the $BaAl_2O_4$ impurity and incomplete sintering may contribute to lower the κ_l to some extent. The κ_l of $x=14$ and 15 almost agrees with each other, and this agreement meets our initial attempt to study the thermoelectric properties of $Ba_8Al_xSi_{46-x}$ systematically as a function of carrier concentration, with other physical quantities unchanged. On the other hand, κ_l of $x=12$ shows much larger values than the other two. Several authors have pointed to the increase of κ_l with the decrease of Al or Ga concentration in $Ba_8Al_xGe_{46-x}$ [50] or $Ba_8Ga_xGe_{46-x}$ [13]. They explained the change of κ_l by the x dependence of structural disorder. From the detailed crystallographic study, it is suggested that the Ba2 position deviates from the center of the cage (6*c*) more distinctly when Al or Ga composition reaches toward $x=16$ [13,50]. The same structural variation may take place for the present system. In Fig. S4 in Supplementary Information, we plotted the x dependence of isotropic atomic displacement parameters U_{iso} for Ba1, Ba2, and Si/Al sites, obtained from the Rietveld fitting. U_{iso} of Ba2 site (6*c* position assumed) shows larger values than those of Ba1 and Si/Al, indicating the site disorder is most prominent for Ba2. With increasing x, U_{iso} of Ba2 shows a tendency to increase. Although our fitting results using powder XRD data taken with a conventional diffractometer is not conclusive, this behavior is similar to those observed for $Ba_8Ga_xGe_{46-x}$ [13] and $Ba_8Al_xGe_{46-x}$ [50] using a synchrotron X-ray or a single-crystal X-ray/neutron diffraction. For the origin of the x variation of κ_l, errors in the estimation of κ_l arising from several assumptions would also be involved.

Temperature dependence of κ_l above 1000 K is weak, and we assume κ_l of $x=15$ above 1000 K to be a constant in order to estimate the thermoelectric property at high temperature. In some cases, κ_l shows a rapid increase at high temperatures because of the crossover to an intrinsic semiconductor region, where both electrons and holes can participate in the thermal conductivity, and the subtraction of κ_e using the Wiedemann–Franz law is no more valid [11]. For the present samples, such crossover to an intrinsic region is not observed in $\alpha(T)$ and $\rho(T)$ up to the highest temperature measured ($\sim$1200 K), thereby the above assumption of linearly extrapolated κ_l is reasonable. The lattice thermal conductivity thus extrapolated, κ_l^{ex}, is used to estimate the extrapolation for total thermal conductivity of $x=15$ by $\kappa_{total}^{ex}=\kappa_l^{ex}+\kappa_e$, which is shown as the dashed line in Fig. 8(a).

The thermoelectric figure of merit is a dimensionless factor defined as $zT=\alpha^2T/\rho\kappa_{total}$. In Fig. 9, the zT obtained from the measured data are shown by markers, while the dashed line for $x=15$ indicates extrapolated zT using κ_{total}^{ex} for $x=15$. zT is found to increase with increasing x, and therefore with decreasing carrier concentration. For $x=15$, the highest zT obtained from measured data is 0.24 at 1000 K, while a zT of 0.31 is expected at $T=1150$ K using the extrapolated thermal conductivity. These values are similar to that of $Ba_8Al_{14}Si_{31}$ as expected given the comparable carrier concentrations and Seebeck coefficients found in the $x=15$ sample and $Ba_8Al_{14}Si_{31}$ [36]. The comparable thermoelectric properties of $Ba_8Al_{14}Si_{31}\square_1$ and $Ba_8Al_{15}Si_{31}$ ($x=15$), despite likely differences in vacancy concentrations, indicate that carrier concentration is the most relevant factor for thermoelectric performance in the Ba–Al–Si clathrates.

Zintl compounds with high thermoelectric efficiency generally have carrier concentrations in the range of 10^{19}–10^{20} cm^{-3} [33,49,51–53]. Here, we use a single parabolic band model to predict the carrier concentration at which zT is optimized in $Ba_8Al_xSi_{46-x}$ at 1000 K. In these calculations, a single effective mass of electron, m^*, and a scattering parameter (λ) of zero are used, while κ_l is assumed to be constant across all carrier concentrations. Effective mass m^* and the intrinsic mobility μ_0 are calculated from

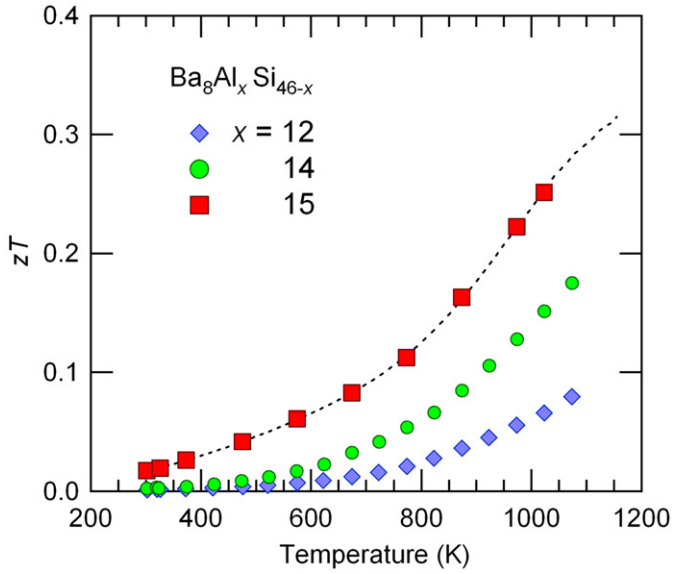

Fig. 9. Figure of merit zT of $Ba_8Al_xSi_{46-x}$. Dashed line is the extrapolation of zT for $x=15$ obtained from the κ_{total}^{ex} and the measured α and ρ.

the following equations,

$$n=4\pi\left(\frac{2m^*k_BT}{h^2}\right)^{3/2}F_{1/2}(\eta), \tag{4}$$

$$\mu=\mu_0\frac{\pi^{1/2}F_\lambda(\eta)}{2\Gamma(1+\lambda)F_{1/2}(\eta)}, \tag{5}$$

where h is the Planck constant, and Γ the gamma function. $m^*=2.7m_e$ (m_e is the electron mass) and $\mu_0=2.2$ cm^2/Vs are obtained from the Eqs. (3)–(5) with the measured α, n, and μ of the $x=15$ sample at 1000 K. The value of m^* is comparable to those obtained for $Ba_8Ga_{16}Ge_{30}$ [17] and $Sr_8Ga_{16}Ge_{30}$ [46]. For the two compounds, m^* has also been estimated from the calculated band structure, yielding $m^*=1.7m_e$ and $3.1m_e$ for $Ba_8Ga_{16}Ge_{30}$ and $Sr_8Ga_{16}Ge_{30}$, respectively [46]. On the other hand, effective mass is not available from the band calculation for $Ba_8Al_{16}Si_{30}$ [39].

Eqs. (1)–(5) are then used to predict the carrier concentration dependence of zT using the equation,

$$zT=\frac{\alpha^2Tne\mu}{\kappa_l+LTne\mu}. \tag{6}$$

The lattice thermal conductivity of the $x=15$ sample are used in Eq. (6).

The result of the calculation is shown in Fig. 10. This model predicts a maximum zT at 1000 K of approximately 0.7 at $n\sim4\times10^{20}$ cm^{-3}. As anticipated, this optimal carrier concentration is significantly lower than those obtained in this study. Thus, it is likely that higher zT values will be obtained if lower electron concentrations can be attained in the $Ba_8Al_xSi_{46-x}$ system. This might be accomplished through synthesis of samples with compositions nearer to the Zintl condition ($Ba_8Al_{16}Si_{30}$), or substitutions such as Zn on the Al site, or K on the Ba sites, etc., to further decrease the free electron concentrations. In addition, higher zT values could be realized if the carrier electron mobility μ is improved by optimizing the sample sintering process. In fact, a simple electron counting for the Al composition $x=15$ should lead the carrier concentration $n\sim9\times10^{20}$ cm^{-3} [12,17], which is much closer to the optimum value than the sample of $x=15$ used in the present study. This indicates there is much room to improve the sample preparation process to reduce the carrier concentration. Therefore more studies are encouraged for the Ba–Al–Si-based type-I clathrates in order to

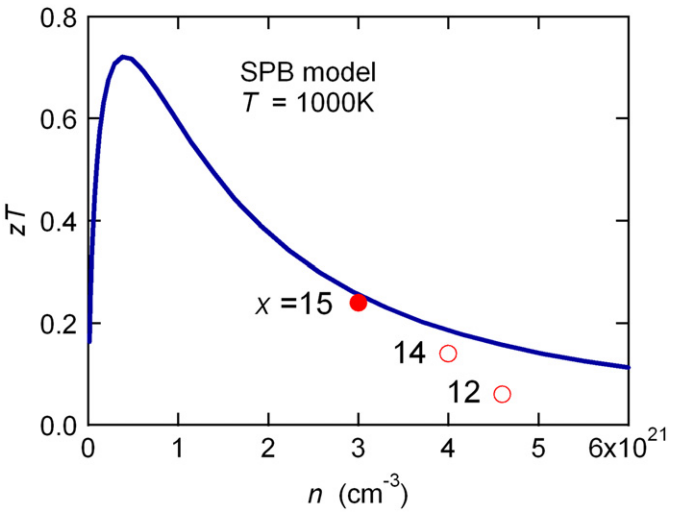

Fig. 10. Calculated figure of merit zT at $T=1000$ K as a function of carrier concentration n for $Ba_8Al_xSi_{46-x}$ system based on the single parabolic band (SPB) model with the assumption of dominant acoustic phonon scattering. Carrier concentration for $x=12$ and 14 are estimated from the electrical resistivity (see text for detail).

capitalize on the advantages of the Ba–Al–Si system such as its thermal stability and the natural abundances of the constituents.

4. Conclusion

Phase stability of the type-I Ba–Al–Si clathrate phases has been investigated. Polycrystalline samples of $Ba_8Al_xSi_{46-x}$ were synthesized by argon arc melting and subsequent annealing at temperatures of 1020–1270 K. Powder X-ray diffraction pattern showed pure type-I clathrate is obtained for the as-cast samples of $x=8$–12, suggesting the compounds with these compositions melt congruently. As-cast sample for $x=16$ showed the existence of several phases including type-I clathrate structure but with much smaller lattice constant, indicating lower Al concentration. Annealing was found to be effective to extend the homogeneity range of the type-I phase. The electron microprobe analysis and chemical composition study demonstrated that the type-I $Ba_8Al_xSi_{46-x}$ phase exists in the chemical composition range of $8 \le x \le 15$. Therefore the existence of the Zintl phase $Ba_8Al_{16}Si_{30}$ is not confirmed. The study indicates that the type-I Ba–Al–Si clathrate compound without framework deficiency does exist in the composition range. The lattice constant was found to obey a linear Vegard's law $a=10.316(12)+0.0208(10)x$. This relation suggests that the $Ba_8Al_{16}Si_{30}$ samples reported to date did not attain the Zintl formulism, which explains the poor thermoelectric performance in the Ba–Al–Si type-I phase.

Thermoelectric measurements have been performed on the SPS pellets of $Ba_8Al_xSi_{46-x}$ samples with $x=12$, 14 and 15. Increased x resulted in improved thermoelectric properties, with a maximum figure of merit $zT\sim0.3$ for $x=15$ at $T=1150$ K. This value is still much lower than that of $Ba_8Ga_{16}Ge_{30}$. This is attributed to the deviation of the chemical composition from the ideal Zintl condition $x=16$, which resulted in the large carrier electron concentration of 3×10^{21} cm^{-3}. Carrier concentration dependence of the Seebeck coefficient and zT have been analyzed by the general expression from the Boltzmann transport equations under the assumptions of single parabolic band and dominant acoustic phonon scattering mechanism. The calculations explained the experimental values quantitatively, and indicates the optimum carrier concentration for the type-I $Ba_8Al_xSi_{46-x}$ compound should be 4×10^{20} cm^{-3}, where $zT=0.7$ is expected at $T=1000$ K. It is vital to reduce the carrier electron number further and increase the carrier mobility to improve the thermoelectric performance of this system. Optimizing the sintering process, and/or partial substitution of Al by Zn or of Ba by K, would be a promising way.

Supplementary information available

Supplementary information can be found in the online version: including powder X-ray diffraction patterns for $Ba_8Al_xSi_{46-x}$ as-cast ($x=16$), annealed ($x=6$–16), and SPS ($x=12$, 14, 15) samples with Rietveld fitting results, values of isotropic atomic displacement parameter U_{iso} obtained by the Rietveld analysis, and the temperature dependence of the carrier concentration of $Ba_8Al_{15}Si_{31}$ SPS sample.

Acknowledgments

This research was funded by NSF, DMR-0600742, and NASA. The work was partly supported by Japan Society for the Promotion of Science (JSPS). The authors gratefully acknowledge Dr. Sarah Roeske and Brian Joy for the microprobe analysis and the Jet Propulsion Laboratory for use of high temperature Hall and Seebeck measurement systems.

Appendix A. Supporting information

Supplementary data associated with this article can be found in the online version at doi:10.1016/j.jssc.2011.03.038.

References

[1] G.A. Slack, in: D.M. Rowe (Ed.), CRC Handbook of Thermoelectrics, Chemical Rubber, Boca Raton FL, 1995, p. 407 Chap. 34.
[2] G.S. Nolas, J.L. Cohn, G.A. Slack, S.B. Schujman, Appl. Phys. Lett. 73 (1998) 178.
[3] J.L. Cohn, G.S. Nolas, V. Fessatidis, T.H. Metcalf, G.A. Slack, Phys. Rev. Lett. 82 (1999) 779.
[4] M. Christensen, S. Johnsen, B.B. Iversen, Dalton Trans. 39 (2010) 978 (For a recent review.).
[5] N.P. Blake, S. Latturner, J.D. Bryan, G.D. Stucky, H. Metiu, J. Chem. Phys. 115 (2001) 8060.
[6] G.K.H. Madsen, K. Schwarz, P. Blaha, D.J. Singh, Phys. Rev. B 68 (2003) 125212.
[7] V.L. Kuznetsov, L.A. Kuznetsova, A.E. Kaliazin, D.M. Rowe, J. Appl. Phys. 87 (2000) 7871.
[8] B.C. Sales, B.C. Chakoumakos, R. Jin, J.R. Thompson, D. Mandrus, Phys. Rev. B 63 (2001) 245113.
[9] L. Bertini, K. Billquist, D. Bryan, M. Christensen, C. Gatti, L. Holmgren, B.B. Iversen, E. Mueller, M. Muhammed, G. Noriega, A.E.C. Palmqvist, D. Platzek, D.M. Rowe, A. Saramat, C. Stiewe, G.D. Stucky, G. Svensson, M. Toprak, S.G.K. Williams, Y. Zhang, in: Proceedings of the 22nd. International Conference Thermoelectrics, 2003, 127.
[10] M. Christensen, G.J. Snyder, B.B. Iversen, in: Proceedings of the 25th International Conference on Thermoelectrics, 2006, 40.
[11] E.S. Toberer, M. Christensen, B.B. Iversen, G.J. Snyder, Phys. Rev. B 77 (2008) 075203.
[12] H. Anno, M. Hokazono, M. Kawamura, J. Nagao, K. Matsubara, in: Proceedings of the 21st International Conference on Thermoelectronics, 2002, 77.
[13] N.L. Okamoto, K. Kishida, K. Tanaka, H. Inui, J. Appl. Phys. 100 (2006) 073504.
[14] T. Uemura, K. Akai, K. Koga, T. Tanaka, H. Kurisu, S. Yamamoto, K. Kishimoto, T. Koyanagi, M. Matsuura, J. Appl. Phys. 104 (2008) 013702.
[15] A. Saramat, G. Svensson, A.E.C. Palmqvist, C. Stiewe, E. Mueller, D. Platzek, S.G.K. Williams, D.M. Rowe, J.D. Bryan, G.D. Stucky, J. Appl. Phys. 99 (2006) 023708.
[16] J. Martin, H. Wang, G.S. Nolas, Appl. Phys. Lett. 92 (2008) 222110.
[17] A.F. May, E.S. Toberer, A. Saramat, G.J. Snyder, Phys. Rev. B 80 (2009) 125205.
[18] M.A. Avila, K. Suekuni, K. Umeo, T. Takabatake, Physica B 383 (2006) 124.
[19] D. Cederkrantz, A. Saramat, G.J. Snyder, A.E.C. Palmqvist, J. Appl. Phys. 106 (2009) 074509.
[20] M.A. Avila, K. Suekuni, K. Umeo, H. Fukuoka, S. Yamanaka, T. Takabatake, Appl. Phys. Lett. 92 (2008) 041901.

[21] N.P. Blake, D. Bryan, S. Latturner, L. Møllnitz, G.D. Stucky, H. Metiu, J. Chem. Phys. 114 (2001) 10063.
[22] B. Eisenmann, H. Schäfer, R. Zagler, J. Less-Common Metals 118 (1986) 43.
[23] A. Bentien, B.B. Iversen, J.D. Bryan, G.D. Stucky, A.E.C. Palmqvist, A.J. Schults, R.W. Henning, J. Appl. Phys. 91 (2002) 5694.
[24] A. Bentien, E. Nishibori, S. Paschen, B.B. Iversen, Phys. Rev. B 71 (2005) 144107.
[25] S.M. Kauzlarich, C.L. Condron, J.K. Wassei, T. Ikeda, G.J. Snyder, J. Solid State Chem. 182 (2009) 240.
[26] A. Hurtado, J.H. Roudebush, N. Tsujii, S.M. Kauzlarich, Spring Meeting of the American Chemical Society, 2010.
[27] M. Imai, K. Nishida, T. Kimura, K. Yamada, J. Alloys Compd. 335 (2002) 270.
[28] W. Carrillo-Cabrera, R. Cardoso Gil, Y. Grin, Z. Kristallogr. NCS 217 (2002) 179.
[29] K. Suekuni, M.A. Avila, K. Umeo, T. Takabatake, Phys. Rev. B 75 (2007) 195210.
[30] K. Kishimoto, N. Ikeda, K. Akai, T. Koyanagi, Appl. Phys. Exp. 1 (2008) 031201.
[31] Y. Mudryk, P. Rogl, C. Paul, S. Berger, E. Bauer, G. Hilscher, C. Godart, H Noël, J. Phys.:Condens. Matter 14 (2002) 7991.
[32] Y. Mudryk, P. Rogl, C. Paul, S. Berger, E. Bauer, G. Hilscher, C. Godart, H. Noël, A. Saccone, R. Ferro, Physica B 328 (2003) 44.
[33] E.S. Toberer, A.F. May, G.J. Snyder, Chem. Mater. 22 (2010) 624.
[34] C.L. Condron, R. Porter, T. Guo, S.M. Kauzlarich, Inorg. Chem. 44 (2005) 9185.
[35] C.L. Condron, J. Martin, G.S. Nolas, P.M.B. Piccoli, A.J. Schultz, S.M. Kauzlarich, Inorg. Chem. 45 (2006) 9381.
[36] C.L. Condron, S.M. Kauzlarich, F. Gascoin, G.J. Snyder, Chem. Mater. 18 (2006) 4939.
[37] C.L. Condron, S.M. Kauzlarich, Inorg. Chem. 46 (2007) 2556.
[38] C.L. Condron, S.M. Kauzlarich, T. Ikeda, G.J. Snyder, F. Haarmann, P. Jeglic, Inorg. Chem. 47 (2008) 8204.
[39] E.N. Nenghabi, C.W. Myles, J. Phys.:Condens. Matter 20 (2008) 415214.
[40] F. Izumi, K. Momma, Solid State Phenom. 130 (2007) 15–20.
[41] K. Momma, F. Izumi, J. Appl. Cryst. 41 (2008) 653.
[42] C.L. Condron, H. Hope, M.B.P. Piccoli, A.J. Schultz, S.M. Kauzlarich, Inorg. Chem. 46 (2007) 4523.
[43] S. Yamanaka, M. Kajiyama, S.N. Sivakumar, H. Fukuoka, High Press. Res 24 (2004) 481.
[44] R.P. Elliott, F.A. Shunk, Bull. Alloy Phase Diagrams 2 (1981) 351.
[45] I.N. Ganiyev, A.V. Vakhobov, T.D. Dzhurayev, Russ. Metall 4 (1978) 183.
[46] I. Fujita, K. Kishimoto, M. Sato, H. Anno, T. Koyanagi, J. Appl. Phys. 99 (2006) 093707.
[47] H.J. Goldsmid, J.W. Sharp, J. Elec. Mater 28 (1999) 869.
[48] C.A. Cox, E.S. Toberer, A.A. Levchenko, S.R. Brown, G.J. Snyder, A. Navrotsky, S.M. Kauzlarich, Chem. Mater. 21 (2009) 1354.
[49] G.J. Snyder, E.S. Toberer, Nature Mater 7 (2008) 105.
[50] M. Christensen, B.B. Iversen, Chem. Mater. 19 (2007) 4896.
[51] A.F. May, J.P. Fleurial, G.J. Snyder, Chem. Mater. 22 (2010) 2995.
[52] E.S. Toberer, A.F. May, B.C. Melot, E. Flage-Larsen, G.J. Snyder, Dalton Trans. 39 (2010) 1046.
[53] E.S. Toberer, S.R. Brown, T. Ikeda, S.M. Kauzlarich, G.J. Snyder, Appl. Phys. Lett. 93 (2008) 062110.